Research Square

Preprints are preliminary reports that have not undergone peer review.
They should not be considered conclusive, used to inform clinical practice,
or referenced by the media as validated information.

Fabrication of SiO2/C composite microwave absorbents derived from corn cob

Yufei Wu
Taiyuan University of Science and Technology
Jinhao Hu
Taiyuan University of Science and Technology
Jinyan Li
Taiyuan University of Science and Technology
Liping Liang
Taiyuan University of Science and Technology
Yirong Huang
Taiyuan University of Science and Technology
Kun Jia
Thirty-third Research Institute of China Electronics Technology Group Corporation
Xiaoqiang Dong
Taiyuan University of Science and Technology
Kewei Zhang
Taiyuan University of Science and Technology
Guomin Li
ligm@tyust.edu.cn

Taiyuan University of Science and Technology

Research Article

Keywords: Corn cob, high-temperature solid-phase reaction, SiO2/C composite, microwave absorption

Posted Date: November 23rd, 2026

DOI: https://doi.org/10.21203/rs.3.rs-11696666/v1

License: This work is licensed under a Creative Commons Attribution 4.0 International License.
Read Full License

Additional Declarations: No competing interests reported.

Fabrication of SiO_2/C composite microwave absorbents derived from corn cob

Yufei Wu [a], Jinhao Hu [a], Jinyan Li [a], Liping Liang [a,*], Yirong Huang [a], Kun Jia [b], Xiaoqiang Dong [a], Kewei Zhang [a], Guomin Li [a,*]

a School of Materials Science and Engineering, Taiyuan University of Science and Technology, 030024 Taiyuan, China

b Thirty-third Research Institute of China Electronics Technology Group Corporation, 030032 Taiyuan, China

*Corresponding author.

E-mail addresses: 1996019@tyust.edu.cn (L. Liang), ligm@tyust.edu.cn (G. Li)

Abstract: Aiming to achieve the high-value resource utilization of agricultural waste, this work focuses on developing low-cost carbon-based microwave absorbents. In this study, corn cobs are employed as the biomass carbon source, and SiO_2/C composites with superior microwave absorption (MA) performance are fabricated via a sol-gel method combined with a high-temperature solid-phase reaction strategy. The evolution laws of calcination temperature and SiO_2 loading content on the microstructure and MA performance of the composites are systematically revealed, and the intrinsic microwave loss mechanism of the composites is clarified. The results demonstrate that the as-prepared SiO_2/C composites possess a unique hierarchical porous microstructure and construct abundant heterogeneous interfaces. For SiO_2/C-900-40, a minimum reflection loss (RL_{min}) of -26.2 dB is achieved at a matching thickness of only 1.5 mm, with a corresponding effective absorption bandwidth (EAB) of 3.84 GHz. Although the SiO_2/C-700-40 sample exhibits slightly inferior graphitization degree, it also delivers exceptional MA performance, with the RL_{min} of -50.7 dB and corresponding EAB of 4.62 GHz. Further analysis reveals that the excellent MA performance SiO_2/C composites originates from the synergistic effects of multiple loss mechanisms and optimized impedance matching. This work not only successfully develops a low-cost carbon-based composite absorbents but also provides valuable insights for the resource utilization of agricultural waste.

Key words: Corn cob, high-temperature solid-phase reaction, SiO_2/C composite, microwave absorption

1. Introduction

With the rapid development of modern electronic information technology and the wide popularization of electronic devices, electronic products have been extensively applied in various fields of society. While these devices bring great convenience to daily life and industrial production, the accompanying electromagnetic pollution has also become increasingly severe [1, 2]. Electromagnetic pollution not only poses a serious threat to human health, but also causes different degrees of interference and damage to the normal operation of electronic equipment [3-5]. Accordingly, developing advanced materials capable of efficiently eliminating harmful electromagnetic radiation has become an urgent demand for addressing these problems. As a typical class of electromagnetic protection materials, microwave absorption materials (MAMs) can convert incident electromagnetic waves into other forms of energy (predominantly thermal energy) and completely dissipate electromagnetic energy via their inherent loss mechanisms, making them the most promising candidates for electromagnetic pollution control [6, 7].

High-performance MAMs are generally required to meet the core characteristics of "wide effective absorption bandwidth, light weight, strong absorption intensity and thin matching thickness". Against this background, carbon-based materials have attracted extensive attention owing to their outstanding advantages including high conductivity, large specific surface area, low density and tunable physicochemical properties [8–10]. However, single-component carbon materials suffer from unsatisfactory thermal stability and excessively high permittivity, which will deteriorate their dielectric properties and impedance matching characteristics, thus limiting their MA performance. To address these issues, some researchers have compounded carbon materials with magnetic components, and the MA performance of the obtained composites has been improved to a certain extent [11-13]. Nevertheless, magnetic components generally suffer from poor environmental stability, long-term exposure to

air will trigger oxidation reactions, leading to gradual performance degradation of MAMs.

To retain the inherent advantages of carbon materials while simultaneously optimizing their MA performance, introducing second-phase components via composite construction remains a highly effective modification strategy [14]. To develop alternatives to ferromagnetic components, researchers have identified SiO_2 as a promising ideal component for regulating the MA performance of carbon-based absorbents. SiO_2 possesses excellent thermal stability, low conductivity, high temperature resistance and low density. After compounding with carbon matrix, it can enhance the multiple reflection and scattering of incident electromagnetic waves, thus effectively improving the MA performance of carbon-based materials [15]. Zang et al. successfully fabricated α-SiC_p/α-SiC_{nw}/SiO_2/C composite MAMs via a carbothermal reduction process combined with a molding method. The composite exhibited excellent MA performance, its RL_{min} reached -18.37 dB at a coating thickness of 1.3 mm, and the EAB reached 4.9 GHz at a thickness of 1.5 mm [16]. Shen et al. prepared Ni/NiO/SiO_2/C composites via an in-situ annealing method and electrospinning technology. The introduced SiO_2 can refine Ni particles, thus optimizing the permittivity. The Ni/NiO/SiO_2/C composite exhibited enhanced MA performance with a RL_{min} of -40.1 dB and an EAB of 5.2 GHz [17]. The above studies fully demonstrate that SiO_2 can adjust the electromagnetic characteristics of composite MAMs, and exhibits broad application prospects in the field of electromagnetic protection.

To conform to the "treating waste with waste" strategy and the concept of green and sustainable development, while reducing the preparation cost of MAMs, corn cob is considered as an ideal precursor for fabricating carbon-based absorbents [18]. As a typical agricultural waste with huge annual output, corn cob exhibits prominent advantages including natural porous microstructure, high carbon content and extremely low cost [19, 20]. More importantly, corn cob-derived carbon-based materials can inherit the inherent porous structure of raw corn cob, which increases the specific surface area. This porous structure not only promotes the multiple reflection and scattering of electromagnetic waves inside the materials and prolongs the

electromagnetic wave propagation path, but also provides abundant pore channels and active sites for the in-situ loading of dielectric modification components [21–23]. However, there are few research reports on the fabrication of SiO_2/C composites using corn cob as the matrix. The structure-activity relationship between the microstructure and MA performance of such composites still lacks systematic investigation, which leads to the lack of systematic theoretical support for the accurate regulation and performance optimization of MAMs.

In this work, agricultural waste corn cob is used as the carbon source, and tetraethyl orthosilicate is selected as the silicon source to fabricate SiO_2/C composite MAMs via a sol-gel method combined with a high-temperature solid-phase reaction strategy. During the experiment, the graphitization degree of the carbon matrix is regulated by tuning the calcination temperature. On this basis, the SiO_2 loading content is further optimized to improve the MA performance of the as-prepared composites. The results demonstrate that the successful loading of SiO_2 significantly enhances the polarization loss and optimizes the impedance matching characteristics, thus endowing the composites with the synergistic loss mechanism. This work provides a feasible strategy for the high-value utilization of agricultural waste and the low-cost large-scale fabrication of high-performance MAMs.

2. Experimental section

2.1 Raw materials

The corn cobs used in this experiment were collected by ourselves, and their specific element contents are listed in Table. S1. Tetraethyl orthosilicate (TEOS, 208.33 g/mol, 0.934 g/cm^3) was used as the silicon source and purchased from Tianjin Damao Chemical Co., Ltd. Anhydrous ethanol (EtOH) and ammonia water ($NH_3 \cdot H_2O$, 25 %) used in the experiment were both purchased from Sinopharm Chemical Reagent Co., Ltd. All the chemical reagents for this experiment were used directly without any purification.

2.2 Preparation process of SiO_2/C composites

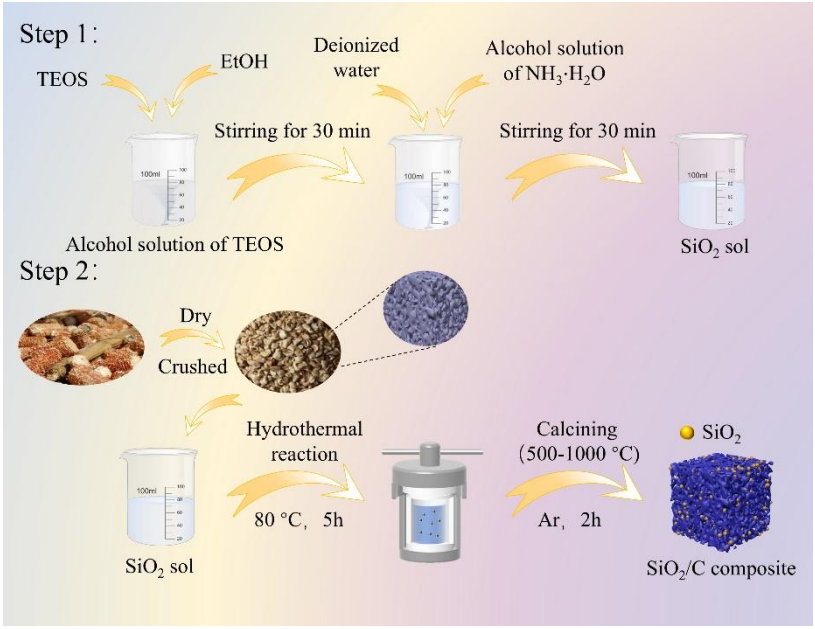

Fig. 1 The synthesis process schematic illustration of SiO_2/C composites

Fig. 1 presents the schematic illustration of the detailed fabrication process for the SiO_2 precursor solution and the as-prepared SiO_2/C composites. Initially, the SiO_2 precursor solution was prepared via a typical sol-gel route [24]. With TEOS adopted as the silicon source, 10 mL of TEOS was mixed with 30 mL of EtOH under continuous stirring until complete dissolution. The mixture was agitated for 30 min to achieve a homogeneous state, after which 1.5 mL of deionized water and 2 mL of $NH_3 \cdot H_2O$ solution were added sequentially. The stirring was maintained for an additional 30 min, ultimately yielding a pale-blue SiO_2 sol precursor solution.

Corn cobs were used as the raw material, and were dried and ground to obtain corn cob powder (denoted as CC). The pretreated CC was added to a certain amount of SiO_2 sol precursor solution for isovolumetric impregnation. The theoretical SiO_2 loading was first fixed at 40 wt% by adjusting the amount of silicon source in the precursor solution. Then, the mixture was transferred into an autoclave, and the reaction was conducted at 80 ℃ for 5 h. After the reaction, the product was placed in a drying oven and dried at

80 ℃ for 5 h. This step removed water and residual solvents from the product, yielding the dry precursor powder. Subsequently, the powder was placed in a tube furnace and calcined at 500-1000 ℃ for 2 h under an argon atmosphere, with a heating rate of 5 ℃/min. Finally, SiO_2/C-*X*-40 (*X* represents the annealing temperature) composites with a SiO_2 loading of 40 wt% and different calcination temperatures were obtained. On the basis of the above experiments, the calcination temperature was further fixed at 900 ℃. With the same preparation process, the theoretical SiO_2 loadings were adjusted to 20 wt% and 60 wt%, respectively, by varying only the amount of SiO_2 sol precursor. Following the same autoclave reaction, drying process and calcination at 900 ℃ for 2 h under an argon atmosphere, SiO_2/C-900-*Y* (*Y* represents the SiO_2 concentration, wt%) composites with different SiO_2 loadings were finally obtained, with the calcination temperature fixed at 900 ℃.

2.3 Material characterization

The phase composition of the samples was analyzed by an X'Pert PRO X-ray diffractometer (XRD, Holland), which operates with Cu Kα radiation at a maximum voltage of 60 kV and covers a 2θ range of 10°~90°. The carbon existing forms in the composites were characterized using a Renishaw-in Via Raman spectrometer (Renishaw, UK) with an excitation wavelength of 532 nm and a spectral range of 500~2000 cm^{-1}. Thermogravimetric (TG) analysis was performed on a TG 309 thermogravimetric analyzer (NETZSCH, Germany) under an argon atmosphere. The as-prepared precursor powder were heated from room temperature to 1000 ℃ at a heating rate of 10 ℃/min to investigate their thermal decomposition process. The microscopic morphology of the SiO_2/C composites was observed using a Hitachi S-4800 scanning electron microscope (SEM, Japan). Meanwhile, the elemental distribution on the sample surface was observed by the energy dispersive spectrometer (EDS) accessory equipped with the SEM. The fine internal crystal structure of the as-prepared samples was characterized using a high-resolution transmission electron microscope (JEM-2100, Japan). An ASAP2020 specific surface area and pore size analyzer (Micromeritics, USA) was employed to characterize the as-prepared samples and obtain the corresponding adsorption-desorption isotherms.

In this experiment, a 85050D model vector network analyzer produced by Agilent Technologies was used to measure the relative complex permittivity and complex permeability of the samples. First, paraffin wax and the samples were mixed uniformly at a mass ratio of 7:3, and then pressed into hollow annular samples with an inner diameter of 3.04 mm and an outer diameter of 7.00 mm. After that, the vector network analyzer was used to measure the electromagnetic parameters of the samples in the range of 2-18 GHz. Formulas (1-3) are the calculation formulas for reflection loss (RL), attenuation ability (α constant) and impedance matching characteristic (Z factor) respectively [25, 26]:

$$RL = 20\lg\left|\frac{Z_{in}-Z_0}{Z_{in}+Z_0}\right| \tag{1}$$

$$\alpha = \frac{\sqrt{2}\pi f}{c}\sqrt{(\mu''\varepsilon'' - \mu'\varepsilon') + \sqrt{(\mu''\varepsilon'' - \mu'\varepsilon')^2 + (\varepsilon'\mu'' + \varepsilon''\mu')^2}} \tag{2}$$

$$Z = \left|\frac{Z_{in}}{Z_0}\right| = \sqrt{\frac{\mu_r}{\varepsilon_r}}tanh\left[j\left(\frac{2\pi f d}{c_0}\right)\sqrt{\mu_r\varepsilon_r}\right] \tag{3}$$

3. Results and discussion

3.1 Effect of calcination temperature on the micro-structure and MA performance of SiO_2/C composites

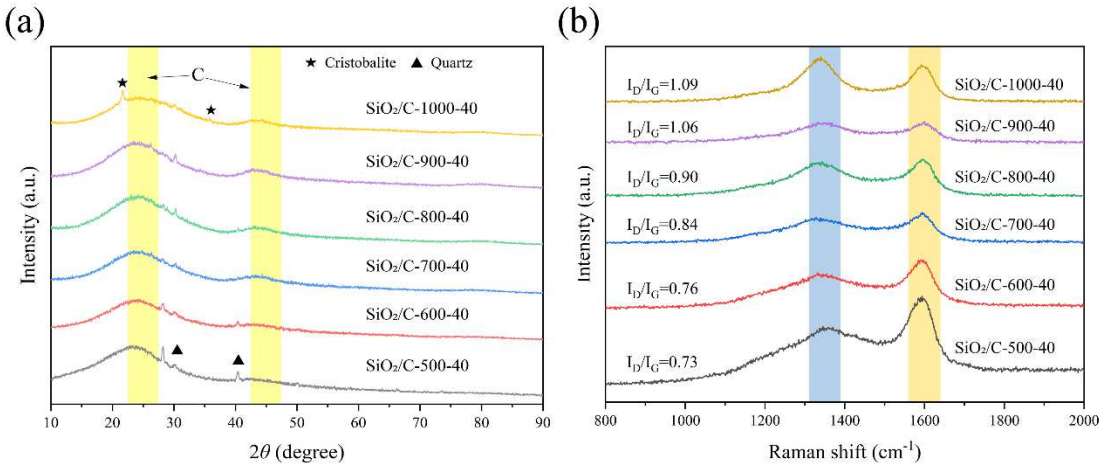

Fig. 2 XRD patterns (a) and Raman spectra (b) of the SiO_2/C-*X*-40 (*X*=500, 600, 700, 800, 900, 1000)

The XRD patterns of the as-prepared samples annealed at different temperatures (500-1000 °C) are presented in Fig. 2(a). For the SiO_2/C samples obtained at 500-900 °C, two diffraction peaks can be observed in the patterns, corresponding to the

characteristic peaks of quartz-phase SiO_2 [27]. This result confirms the successful loading of SiO_2 on the surface of the CC matrix through the impregnation of SiO_2 precursor solution with corn cob powder and subsequent carbonization reaction. For the SiO_2/C-1000-40 sample, two new characteristic diffraction peaks of SiO_2 emerge at 2θ = 21.98° and 35.60°, which are assigned to the more stable cristobalite phase [28]. This indicates that the crystal phase of SiO_2 transforms with increasing temperature, and no chemical reaction occurs to generate new substances within this temperature range. Notably, the diffraction peak around 26.5° is an overlapping peak between the carbon matrix and SiO_2, which cannot directly distinguish the existing state of carbon [29]. Therefore, Raman spectroscopy was employed to further analyze the structural evolution of the carbon matrix.

The Raman spectra for SiO_2/C composites are presented in Fig. 2(b). It can be clearly observed that all samples exhibit two distinct characteristic peaks at 1350 cm^{-1} and 1590 cm^{-1}, corresponding to the D band and G band of carbon, respectively. The D band originates from the A_{1g} vibrational mode of carbon atoms, which reflects the degree of structural defects and disorder in the carbon matrix. The G band is mainly attributed to the E_{2g} phonon stretching vibration of graphitic carbon, representing the in-plane stretching vibration of sp^2-hybridized carbon atoms in graphite [30-32]. Generally, the intensity ratio of the D band to the G band (denoted as R value) is adopted to evaluate the graphitization degree of carbon materials . A smaller R value indicates fewer structural defects and a higher graphitization degree of the carbon material [33]. As shown in Fig. 2b, the R values of the samples annealed at different temperatures are 0.73, 0.76, 0.84, 0.90, 1.06 and 1.09, respectively. According to the three-stage model theory, as the intensity ratio of the D band to the G band (I_D/I_G) first increases and then gradually decreases to 0, the carbon structure undergoes corresponding transformation [34]. Therefore, with the increase of annealing temperature, the R value of the sample increases, indicating that the carbon in the sample transforms from amorphous carbon to nanocrystalline graphite, accompanied by an increase in structural defects [35].

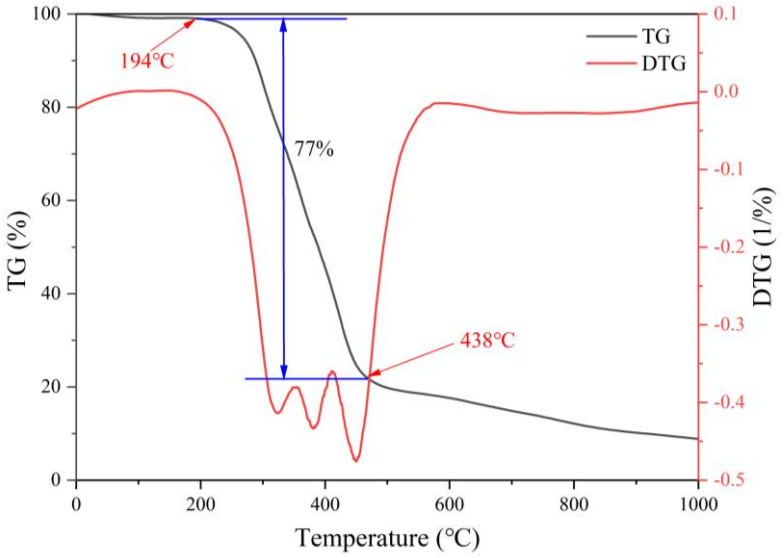

Fig. 3 TG-DTG curves of SiO_2/C precursor powder under Ar atmosphere

To clarify the thermal decomposition behavior of the composite during thermal treatment, TG-DTG characterization was performed on the uncalcined SiO_2/C precursor, and the corresponding results are shown in Fig. 3. The curves clearly reveal the thermal decomposition pattern of the uncalcined SiO_2/C precursor, and the entire thermal weight loss process can be classified into three distinct stages. In the low-temperature range from room temperature to 194 ℃, only slight weight loss is detected, which is mainly ascribed to the elimination of surface-adsorbed water and trace volatile impurities. Meanwhile, partial free silanol groups (Si-OH) in the silicon-based precursor undergo initial dehydration condensation reactions at this stage [36]. No organic components decompose during this period, and the overall structure of the sample remains relatively stable. In the temperature range of 194-438 ℃, the sample exhibits rapid weight loss with a maximum mass loss as high as 77%. This stage corresponds to the intense thermal decomposition of organic components derived from corn cob biomass, including cellulose, hemicellulose and lignin, accompanied by the release of small-molecule gases such as CO, H_2 and CH_4, which ultimately accounts for the sharp decline of the TG curve [37]. On the other hand, the silicon-based

precursor undergoes critical structural evolution in this temperature interval, during which abundant silanol groups (Si-OH) participate in deep dehydration polycondensation reactions and gradually form a three-dimensional inorganic network with Si-O-Si bonds as the backbone [38]. The silicon-based component transforms from an organic-inorganic hybrid gel state to an amorphous SiO_2 structure. The temperature ranges of these two reaction types are highly overlapped, collectively giving rise to the multiple DTG characteristic peaks at this stage. When the temperature exceeds 438 ℃, the weight loss rate slows down significantly, as the main volatile components are completely decomposed and the thermal process is dominated by the carbonization reaction. Meanwhile, the SiO_2 network enters a slow densification stage. Residual trace silanol hydroxyl groups continue to be removed, the Si-O-Si network is further perfected, and the amorphous SiO_2 structure gradually stabilizes [39]. The reaction process is illustrated in Equations (1):

$$\text{Si-OH} + \text{HO-Si} \rightarrow \text{Si-O-Si} \quad (1)$$

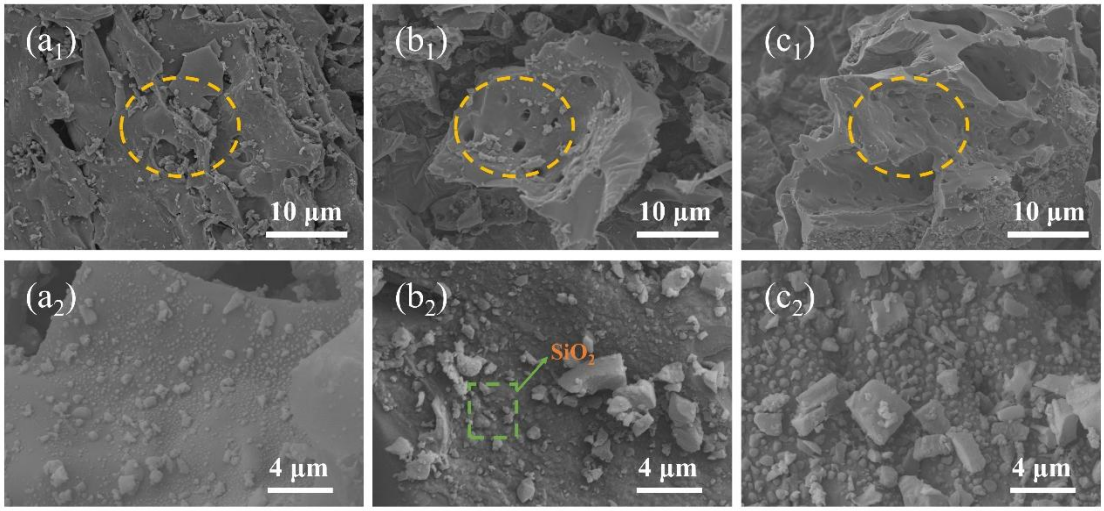

Fig. 4 SEM images of samples: SiO_2/C-700-40 (a_1, a_2), SiO_2/C-800-40 (b_1, b_2), SiO_2/C-900-40 (c_1, c_2)

To further observe the microstructure and component distribution of SiO_2/C composites prepared at different annealing temperatures, three representative samples (SiO_2/C-700-40, SiO_2/C-800-40, and SiO_2/C-900-40) were selected for the SEM characterization. As shown in Fig. 4(a), compared with the blank CC (Fig. S1), the sample still retains the original lamellar porous structure of CC, but exhibits a rough

surface and reduced pore number. Meanwhile, abundant nanoparticles are observed on the surface of the carbon matrix. Combined with the XRD results, these spherical particles are confirmed to be SiO_2. As shown in Fig. 4(b)-4(c), with the increase of annealing temperature, the carbonization reaction is intensified, and the number of internal pores in the sample increases. The increased pore quantity effectively reduces the overall density of the material, which increases the reflection and scattering times of incident electromagnetic waves and significantly prolongs their propagation path, thus enhancing the MA performance [40, 41]. Meanwhile, slight agglomeration of SiO_2 particles can be observed, which are tightly anchored on the surface of the carbon skeleton and pore edges. The formation of such heterogeneous interfaces is crucial for the generation of interfacial polarization [42].

EDS elemental mapping images of the SiO_2/C-700-40 and SiO_2/C-800-40 are presented in Fig. S2. As can be observed from the mapping results, the SiO_2/C composite is mainly composed of C, O, and Si elements, which are uniformly distributed throughout the carbon matrix. Meanwhile, the distribution regions of Si and O elements are highly overlapped, which further verifies that SiO_2 particles are successfully anchored on the CC matrix.

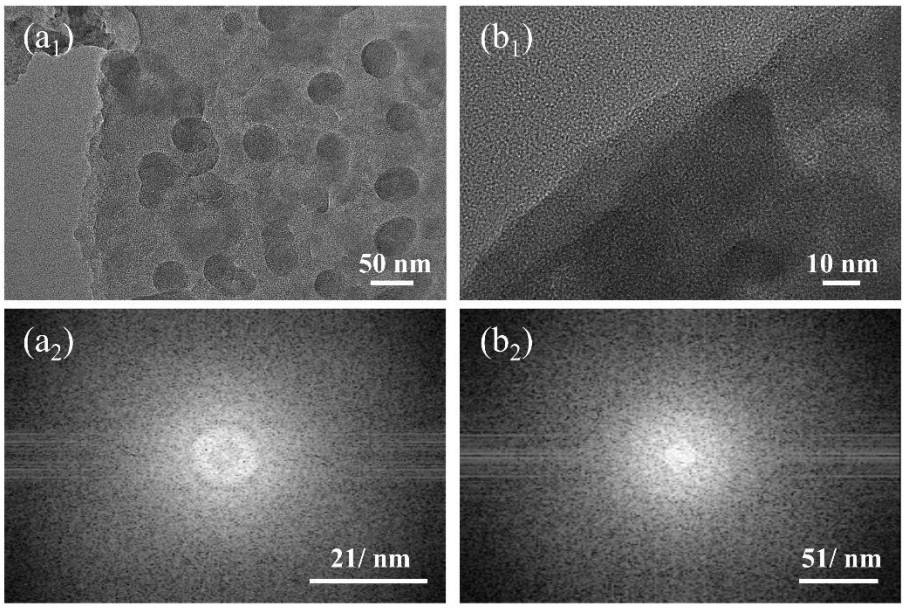

Fig. 5 TEM images of the SiO_2/C-900-40 (a_1), high-resolution TEM images (b_1), selected area electron diffraction spectrum of SiO_2/C-900-40 (a_2-b_2)

To further confirm the microstructure of the composites, the samples were

characterized using TEM. As shown in Fig. 5(a_1), a large number of near-spherical SiO_2 nanoparticles loaded on the irregular sheet-like carbon matrix can be clearly observed in this field of view. The overall dispersion is relatively uniform without large-scale agglomeration. Meanwhile the carbon matrix and SiO_2 particles are tightly bonded at the interface, exhibiting a distinct and continuous two-phase boundary. This verifies the favorable heterogeneous coupling effect, and the resulting abundant SiO_2/C heterogeneous interfaces provide a solid structural foundation for dielectric loss [43,44]. According to the high-resolution transmission electron microscopy (HRTEM) image (Fig. 5(b_1)), the sample overall exhibits disordered and granular contrast characteristics. No distinct and continuous long-range ordered lattice fringes are detected. Only weak and discontinuous short-range ordered contrast can be observed in extremely few nanoscale regions, corresponding to an extremely low proportion of nanoscale graphite crystallites in the carbon matrix [45]. Furthermore, the selected area electron diffraction (SAED) pattern (Fig. 5(a_2)-(b_2)) exhibits the characteristics of a central bright transmitted spot surrounded by diffuse and blurred diffraction rings. Neither clear diffraction spots typical of crystalline materials nor sharp diffraction rings characteristic of crystalline graphite appear [46, 47]. This confirms that the sample is dominated by an amorphous structure overall, with extremely low carbon crystallinity, and SiO_2 also maintains an amorphous state [48]. This is consistent with the structural feature that biomass carbon has not been fully graphitized at the calcination temperature of 900 ℃. The amorphous carbon structure generally contains abundant edge defects, vacancy defects and hybridization distortion sites [49, 50]. These carbon defects can serve as active centers for dipole polarization, providing a structural basis for the dielectric loss of the absorbents [51, 52]. In the Raman spectra, both the D band and G band of SiO_2/C-900-40 exhibit obvious broadening rather than the sharp and narrow peaks of crystalline graphite, further corroborating that the carbon matrix is dominated by a highly defective turbostratic structure with extremely low long-range order degree [53, 54].

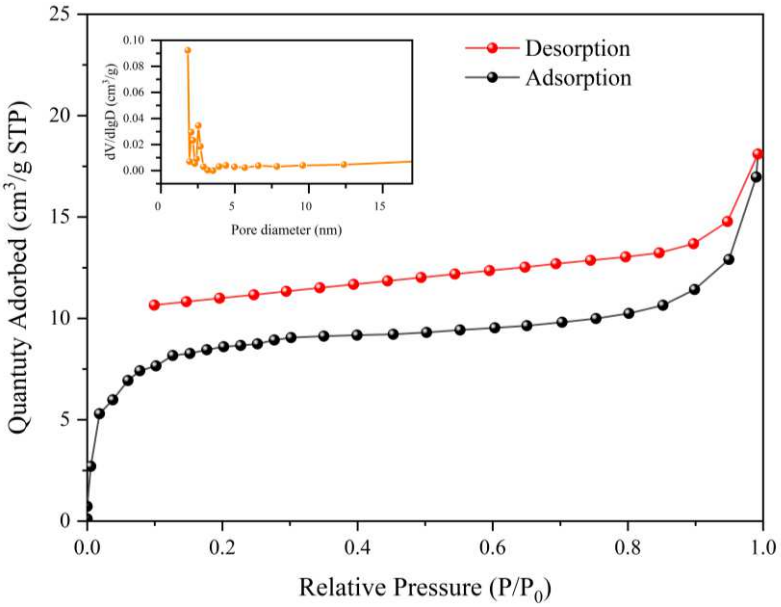

Fig. 6 N_2 adsorption-desorption isotherms of the SiO_2/C-700-40 (the inset is pore size distribution)

To further characterize the pore structure features of the as-prepared samples, Fig. 6 displays the N_2 adsorption-desorption isotherms and corresponding BJH pore size distribution curves of the SiO_2/C-700-40. The sample exhibits typical IUPAC Type IV isotherm characteristics, with an obvious hysteresis loop between the adsorption and desorption branches, which matches the adsorption behavior of mesopore-dominated hierarchical porous materials [55]. The pore size distribution results reveal that the pore structure of the sample is mainly composed of mesopores, accompanied by a small number of micropores and macropores, with an average pore diameter of 3.2 nm. The sample possesses a moderate specific surface area (33 m^2/g) and pore volume (0.026 cm^3/g). The abundant mesoporous structure can prolong the propagation path of electromagnetic waves via multiple scattering and provide abundant interfacial polarization sites, synergistically enhancing the dielectric loss capability [56]. Therefore, the as-prepared sample has great potential to become a high-performance MAMs with the core characteristics of "thin matching thickness, light weight, wide effective absorption bandwidth and strong absorption intensity".

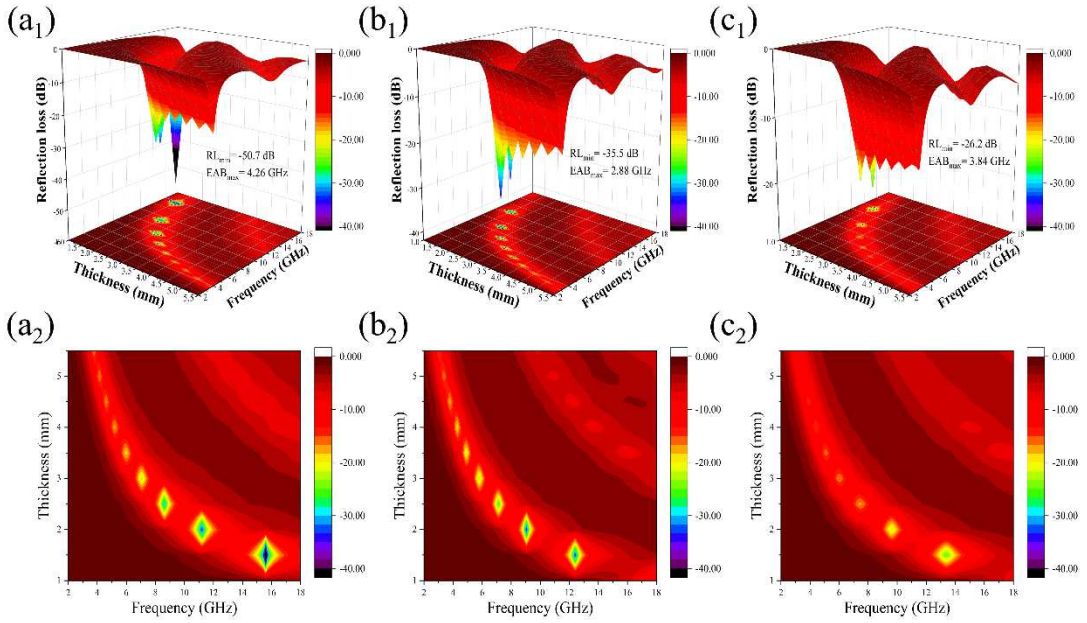

Fig. 7 The 3D and 2D reflection loss plots of samples: SiO_2/C-700-40 (a_1,a_2), SiO_2/C-800-40 (b_1,b_2), SiO_2/C-900-40 (c_1,c_2)

The MA performance of the absorbents is generally evaluated by RL and EAB [57, 58]. Conventionally, an RL value lower than -10 dB is regarded as the criterion for effective microwave absorption, and the frequency range corresponding to RL ≤ -10 dB is defined as EAB [59, 60]. Fig. 7 presents the RL curves of the three samples at different matching thicknesses (1.0-5.5 mm). As can be observed from the Fig. S3, the sample heat-treated at 600 °C exhibits a RL_{min} of only approximately -4 dB, with no effective absorption bandwidth, indicating poor MA performance. With the increase of treatment temperature, the graphitization degree increases, which enhances the conductive loss, thus significantly improving the MA performance of the sample [61, 62]. For the SiO_2/C-700-40 composite, the RL_{min} reaches -50.7 dB at a matching thickness of 1.5 mm, with a corresponding EAB_{max} of 4.62 GHz. However, the MA performance of the samples treated at 800 °C and 900 °C decreases slightly. At a matching thickness of 1.5 mm, the SiO_2/C-800 delivers a RL_{min} of -35 dB, exhibiting superior absorption intensity, yet its EAB_{max} is merely 2.8 GHz. In comparison, the SiO_2/C-900 at the identical matching thickness exhibits an RL_{min} of -26.2 dB, while its corresponding EAB_{max} reaches up to 3.84 GHz, demonstrating a broader effective absorption frequency range. Combined with the SEM analysis, this phenomenon may be attributed to the excessive heat treatment temperature, which causes excessive

consumption of the carbon matrix .

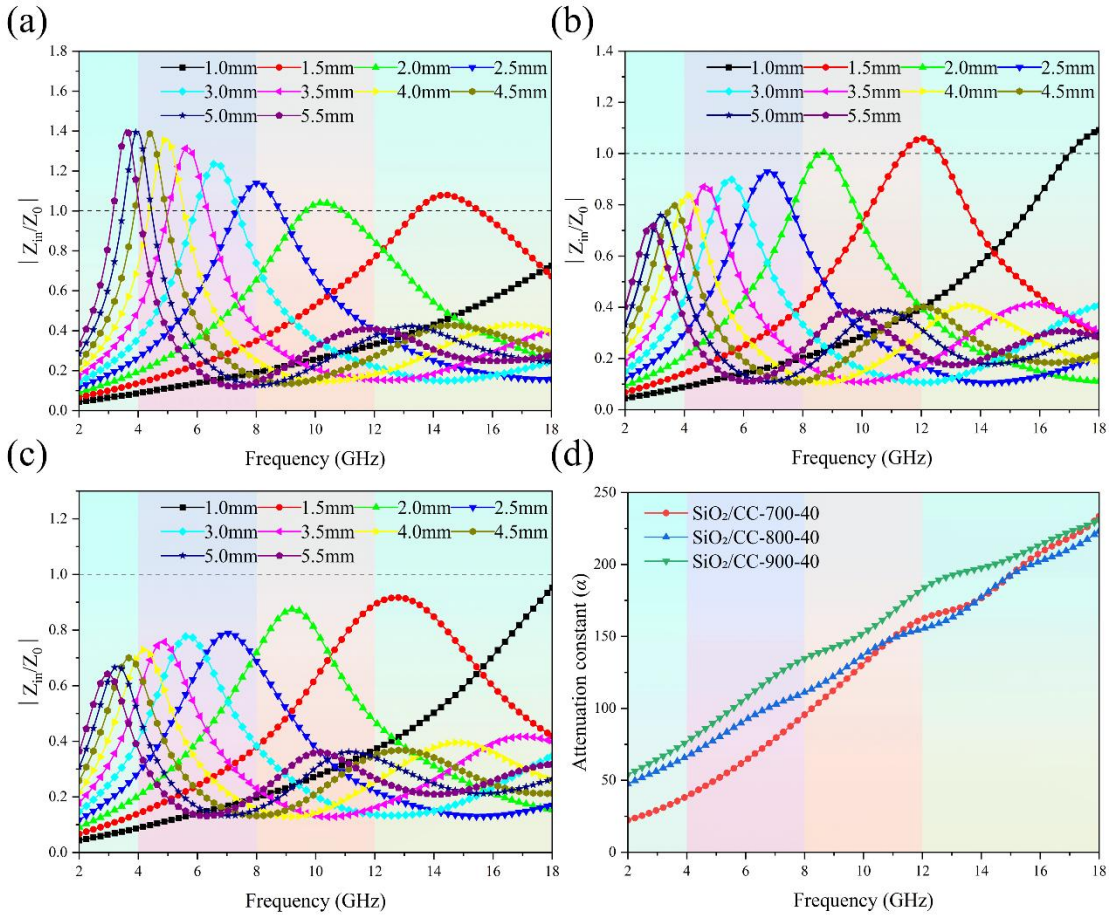

Fig. 8 *Z* factor contour maps (a-c) of samples: SiO_2/C-700-40 (a), SiO_2/C-800-40 (b), SiO_2/C-900-40 (c), and attenuation constant (α) curves (d)

According to the transmission line theory, the MA performance of absorbents is mainly determined by two key factors: the impedance matching and attenuation characteristics [63]. Excellent impedance matching can minimize the reflection of electromagnetic waves upon contacting the material surface, enabling more electromagnetic waves enter into the material interior, while the excellent attenuation characteristics ensure the incident electromagnetic waves can be effectively dissipated [64]. As shown in Fig. 8(a)-8(c), the impedance matching curves of different samples as a function of frequency are presented, and the attenuation constant curves of the samples are also displayed in Fig. 8(d). The *Z* value is adopted to evaluate the impedance matching, a *Z* value closer to 1 indicates better impedance matching characteristic [65, 66]. As can be observed, the *Z* values of SiO_2/C-700-40, SiO_2/C-800-40, and SiO_2/C-900-40 at their corresponding RL_{min} frequencies are close to 1,

indicating that all these samples possess excellent impedance matching characteristics. From the attenuation constant curves, the α value of SiO_2/C-900-40 is higher than that of other samples in the whole test frequency band (2-18 GHz), indicating that it has the strongest electromagnetic wave attenuation capability.

To further explore the MA mechanism of SiO_2/C composites, the relative complex permittivity (ε_r) and complex permeability (μ_r) of the samples were characterized. Since no magnetic components are introduced in the SiO_2/C composites, only the variation of complex permittivity needs to be analyzed. The real part (ε') of complex permittivity represents the electric energy storage capacity of the material, while the imaginary part (ε'') represents the electric energy loss capacity [67, 68]. Fig. 9 presents the variation curves of the real and imaginary parts of complex permittivity for the four samples. As can be clearly observed from Fig. 9(a)-9(b), the ε' and ε'' values of all samples show a decreasing trend with increasing frequency, which is attributed to the typical frequency dispersion effect of electromagnetic waves [69, 70]. Meanwhile, with the increase of calcination temperature, the ε' and ε'' values of the samples increase. This is because the elevated temperature intensifies the carbonization reaction, generating abundant carbon defects after the reaction, which enhances dipole polarization. In addition, the abundant heterogeneous interfaces formed by SiO_2 particles loaded on the carbon matrix also enhance interfacial polarization [71].

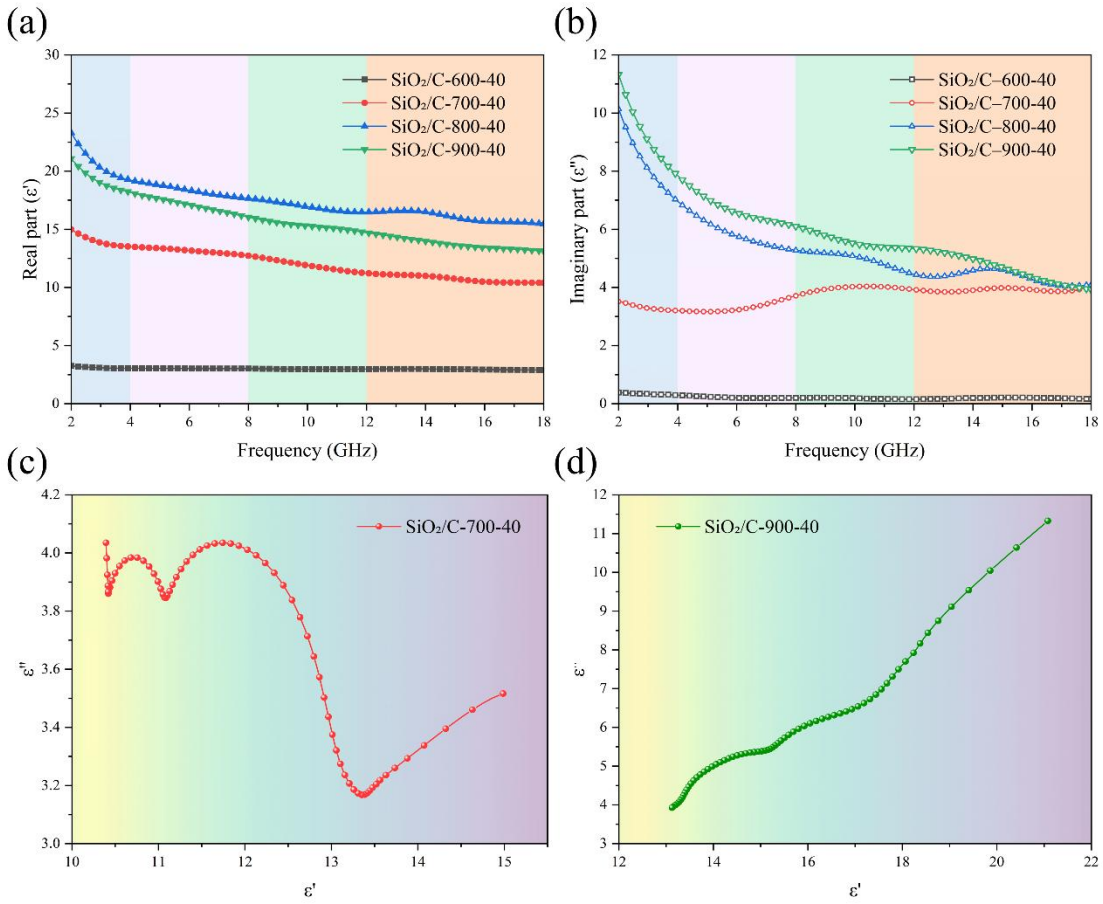

Fig. 9 The ε' (a) and ε'' (b) of the dielectric constant of SiO_2/C-*X*-40 (*X*=600, 700, 800, 900), and the Cole-Cole curves of the SiO_2/C-*X*-40: *X* = 700 (c); *X*=900 (d)

To further investigate the main modes of dielectric loss in the composites, Fig. 9(c)-9(d) presents the Cole-Cole curves of SiO_2/C-700-40 and SiO_2/C-900-40. According to the Debye relaxation theory, each semicircle corresponds to one polarization relaxation process, which originates from the synergistic interaction of dipole polarization and interfacial polarization in the composite [72-74]. Specifically, the polarization relaxation is induced by the combined action of dipole polarization and interfacial polarization in the composites. The dipole polarization originates from carbon defects generated during the calcination-induced carbonization reaction, while the interfacial polarization is attributed to the abundant heterogeneous interfaces formed between the conductive carbon matrix and insulating SiO_2 within the material [75]. The tail regions of both Cole-Cole curves exhibit an obvious linear upward characteristic, which corresponds to the contribution of conductive loss, originating from the long-range migration and local hopping of charge carriers in the carbon-based conductive network [76, 77]. By comparing the samples prepared at two calcination

temperatures, it can be found that the semicircle radius of the 900 ℃ sample is significantly larger than that of the 700 ℃ sample, and the rising slope of the tail linear segment is higher. Further analysis combined with Raman spectroscopy results indicates that with the increase of calcination temperature, the graphitization degree of the carbon matrix is enhanced. It not only strengthens the polarization loss through defect evolution and interface effect, but also greatly improves the conductive loss capability by constructing a more complete conductive network [78]. In summary, the dielectric loss of SiO_2/C composites is the result of the synergistic effect of dipole polarization, interfacial polarization and conductive loss.

3.2 Loading optimization of SiO_2 in SiO_2/C composites

Through the above research and analysis, the sample treated at 900 °C possesses the highest graphitization degree, with the carbonization process basically completed. Therefore, 900 °C is determined as the optimal heat treatment temperature for SiO_2/C composites, and a series of SiO_2/C-900-*X* samples (*X* = 20, 40, 60) are fabricated by adjusting the SiO_2 loading content. The regulation effects of SiO_2 loading on the phase composition, microstructure, and MA performance of the composites are systematically investigated, and the structure-activity relationship between loading content and MA performance is established to clarify the optimal loading range.

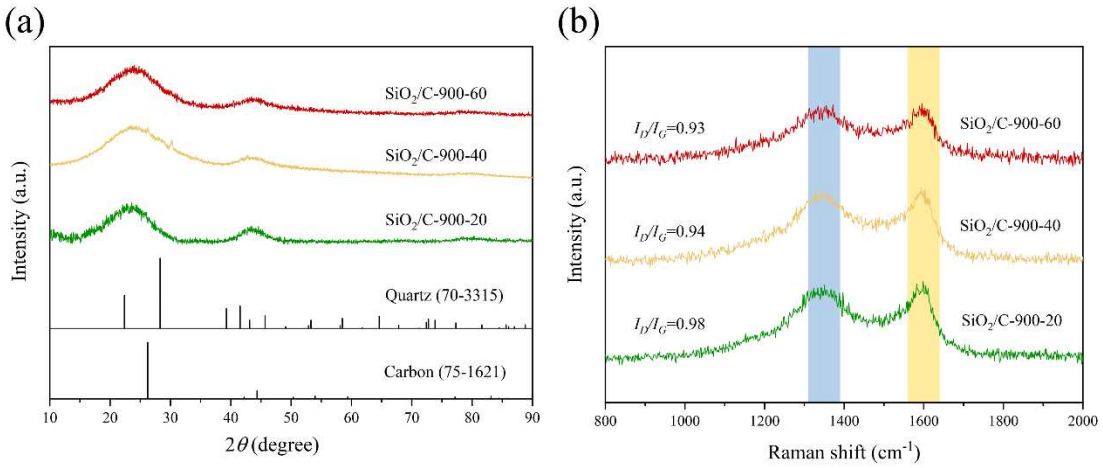

Fig. 10 XRD patterns (a) and Raman spectra (b) of the SiO_2/C-900-*Y* (*Y*=20, 40, 60)

Fig. 10(a) presents the XRD patterns of samples with different SiO_2 loading contents. As can be observed from the patterns, all samples exhibit distinct characteristic diffraction peaks of graphitized carbon near 2θ = 26.5°, indicating that

corn cob has been successfully converted into a carbon matrix with a certain graphitization degree after high-temperature carbonization at 900 °C. Meanwhile, the appearance of characteristic diffraction peaks corresponding to SiO_2 in the patterns further confirms the successful fabrication of the target composites. Owing to the partial overlap of the diffraction peaks between carbon and SiO_2, the carbon defect degree cannot be accurately evaluated only by XRD, thus the Raman spectroscopy is employed for further analysis.

The Raman spectra of SiO_2/C-900-*X* (*X* = 20, 40, 60) are shown in Fig. 10(b). With the increase of SiO_2 loading content, the intensity ratio of D band to G band (I_D/I_G) decreases slightly from 0.98 to 0.93. This is attributed to that the increased loading content leads to the coverage of defect sites on the carbon matrix surface by SiO_2 particles, resulting in a relative reduction of the overall structural disorder degree. Meanwhile, it also inhibits the transformation from amorphous carbon to nanocrystalline graphite, thus lowering the graphitization degree. Notably, the I_D/I_G values of samples with different loadings remain in the range of 0.9-1.0, demonstrating that the samples still retain abundant carbon defects and provide sufficient dipole polarization centers for dielectric loss [79].

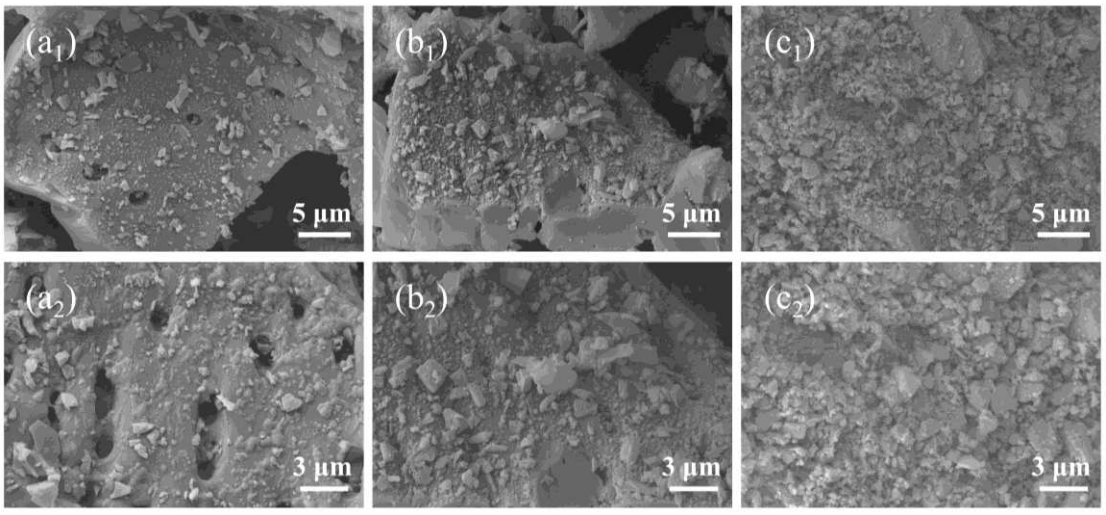

Fig. 11 SEM images of samples: SiO_2/C-900-20 (a_1, a_2), SiO_2/C-900-40 (b_1, b_2), SiO_2/C-900-60 (c_1, c_2)

To further characterize the microstructure of the as-prepared samples, Fig. 11 presents the SEM images of samples with different SiO_2 loading contents. At low loading content, the inherent porous structure of the carbon matrix is well preserved,

and SiO_2 particles are sparsely dispersed on the carbon matrix surface and internal pore channels. When the loading content increases to 40 wt%, the number of SiO_2 particles increases remarkably. SiO_2 particles are uniformly and densely anchored on the carbon matrix surface, forming abundant heterogeneous interfaces, which provides a favorable structural foundation for interfacial polarization. As the loading content further increases to 60 wt%, excessive SiO_2 particles exhibit severe agglomeration and block the internal pores of the carbon matrix, destroying the inherent porous structure derived from corn cob. The EDS elemental mapping results of SiO_2/C-900-*X* (*X* = 20, 60) samples shown in Fig. S4 further verify the uniform distribution of Si and O elements throughout the samples, reconfirming the successful combination of SiO_2 and the carbon matrix.

Fig. 12(a)-12(c) present the curves of reflection loss and impedance matching versus test frequency for the samples at different matching thicknesses. For the SiO_2/C-900-20, the RL_{min} reaches -23.5 dB at a matching thickness of 1.5 mm, with an EAB_{max} of 3.76 GHz. With the increase of SiO_2 loading content, the SiO2/C-900-40 achieves an RL_{min} of -26.2 dB at a matching thickness of 1.5 mm, with a corresponding EAB_{max} of 3.84 GHz. Meanwhile, its *Z* value fluctuates closely around 1, indicating further improved MA performance. In contrast, the SiO_2/C-900-60 obtains an RL_{min} as low as -38.1 dB at a matching thickness of 2.0 mm, while its EAB_{max} is only 3.12 GHz. As shown in Fig. 12(d), the electromagnetic attenuation capability of SiO_2/C-900-40 is slightly superior to that of SiO_2/C-900-20 and SiO_2/C-900-60. Therefore, SiO_2/C-900-40 possesses the optimal comprehensive MA performance, realizing excellent synergistic effect between impedance matching and electromagnetic attenuation capability. This is attributed to that the loading content of 40 wt% provides sufficient effective heterogeneous interfaces and polarization loss active sites, and relatively retaining the inherent porous structure. In contrast, severe SiO_2 agglomeration in SiO_2/C-900-60 blocks internal pore channels and destroys the porous structure, thus weakening both polarization loss and multiple reflection loss [80].

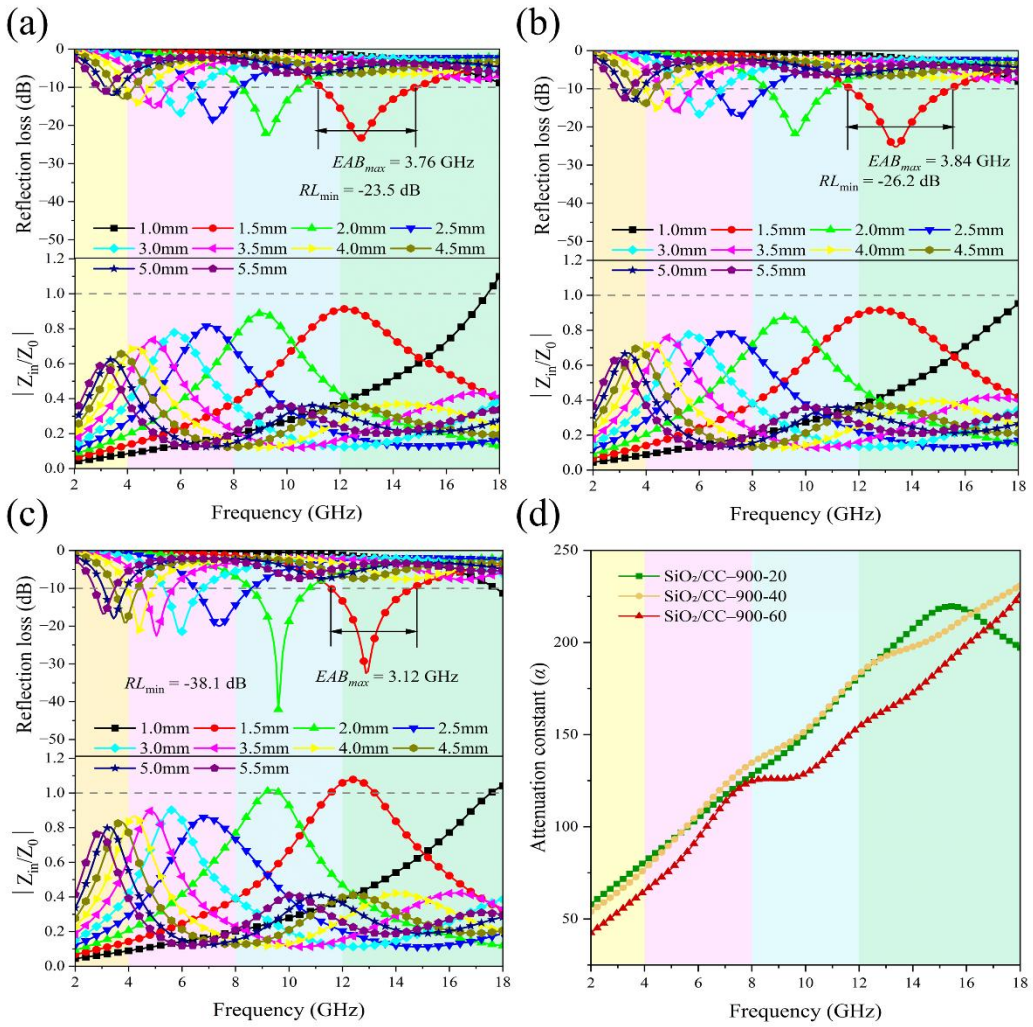

Fig. 12 Reflection loss, impedance-matching characteristic (Z) for SiO_2/C-900-Y (Y = 20, 40, 60): SiO_2/C-900-20 (a), SiO_2/C-900-40 (b), SiO_2/C-900-60 (c) and attenuation constant (α) curves (d)

In brief, appropriate regulation of calcination temperature and SiO_2 loading content not only constructs abundant heterogeneous interfaces, but more importantly, effectively optimizes the impedance matching characteristics of high-conductivity carbon materials. Fig. 13 summarizes the MA performance of typical recently reported MA absorbents [81-84]. The results demonstrate that the optimized SiO_2/C composite exhibits superior MA performance, combined with the merits of a facile fabrication process and low cost. This indicates that the SiO_2/C system is a highly promising lightweight and high-efficiency MAMs.

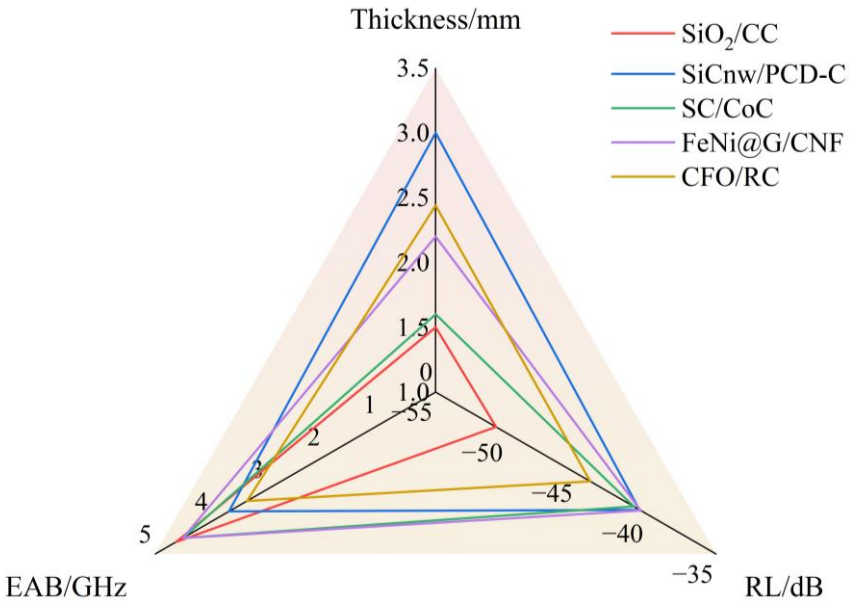

Fig. 13 MA characteristics of similar absorbents in the literatures

3.3 MA mechanism of SiO_2/C composites

The MA mechanism of the SiO_2/C composites is schematically illustrated in Fig. 14. First, the composites retain the inherent porous structure of the CC matrix after a series of chemical reactions, which significantly enhances the multiple reflection and scattering of incident electromagnetic waves within the SiO_2/C composites. Meanwhile, the carbon defects generated during the high-temperature carbonization process provide abundant dipole sites, which induces dipole polarization and generates relaxation attenuation of incident electromagnetic waves, effectively improving the electromagnetic wave dissipation capability [85, 86]. Second, the graphitized carbon in the composite constructs a continuous three-dimensional conductive network, which can effectively promote the migration and hopping of charge carriers, resulting in significant conductive loss - a key component of the dielectric loss of the composite [87, 88]. SiO_2 particles are uniformly anchored on the surface of the carbon matrix, forming abundant heterogeneous interfaces in the system. The significant difference in conductivity and permittivity at the interfaces leads to space charge accumulation, generating strong interfacial polarization and relaxation effects, which further enhance the dielectric loss of electromagnetic waves [89, 90]. In summary, benefiting from the synergistic effect of multiple loss mechanisms, the SiO_2/C composites exhibit excellent MA performance.

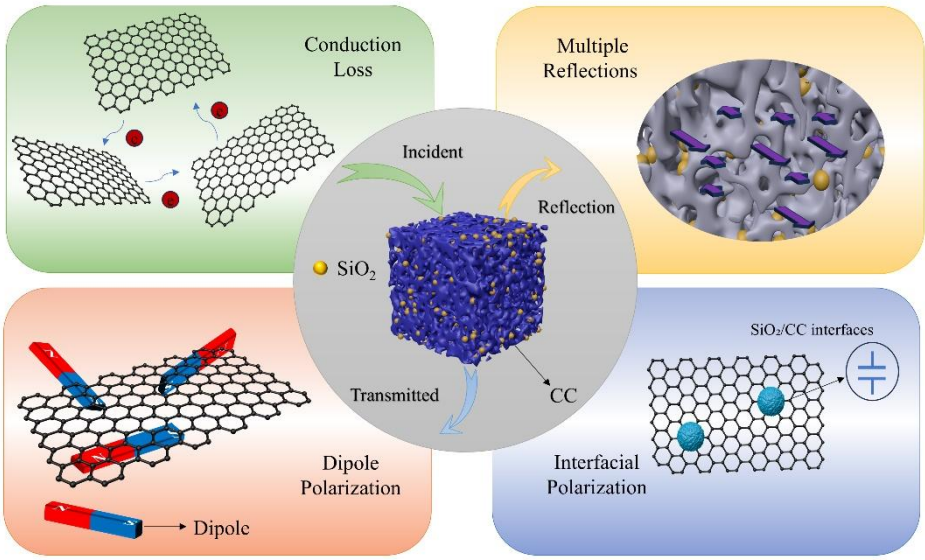

Fig. 14 Schematic illustration of the MA mechanism for SiO_2/C composites

4. Conclusion

In this work, SiO_2 particles were successfully loaded on the surface of corn cob-derived carbon matrix (CC) via a sol-gel method combined with a high-temperature solid-phase reaction strategy, and SiO_2/C composites were finally fabricated. Meanwhile, the effects of calcination temperature and SiO_2 loading on the MA performance of the composites were systematically investigated. When the calcination temperature is 700 °C, the sample achieves a RL_{min} of -50.7 dB at 15.6 GHz with a matching thickness of only 1.5 mm, and the corresponding EAB_{max} reaches 4.62 GHz (13.6-18 GHz). When the calcination temperature is 900 °C, the sample exhibits an RL_{min} of -26.2 dB at a thickness of 1.5 mm, with a corresponding EAB_{max} of 3.84 GHz. Reasonable regulation of SiO_2 loading can adjust the number of heterogeneous interfaces in the composites. However, excessive loading will lead to agglomeration on the carbon matrix surface, which deteriorates the MA performance. Ultimately, this work not only realizes the high-value functional utilization of corn cob, but also solves the problems of resource waste and environmental pollution caused by the random disposal of biomass waste. Furthermore, it provides a new technical route and experimental basis for the low-cost and large-scale preparation of biomass carbon-based composite MA absorbents.

Data availability

Data will be made available on request.

References

[1] Q.D. Tran, D.V. Le, T.H. Nguyen, N.L. Nguyen, T.L. To, D.L. Vu, N. Tran, Tunable microwave absorption of bio-carbon/CuFe2O4: a trade-off for broadband versus stealth performance, Ceram. Int. (2025). https://doi.org/10.1016/j.ceramint.2025.12.220.

[2] R. Qiang, Y. Ding, Y. Shao, L. Rong, D. Zhang, R. Hao, R. Xue, N. Xiao, H. Liu, J. Qiu, Construction of one-dimensional hierarchical MoO2/C with dominant dielectric loss for microwave absorption, J. Alloys Compd. (2026). https://doi.org/10.1016/j.jallcom.2026.186343.

[3] N. Zhai, Z. Wang, Z. Cheng, L. Xu, W. Yang, W. Zhou, F. Gao, X. Zeng, G. Luo, MoS2/rGO/MXene/TiO2 composite aerogel with enhanced Mott-Schottky effect for achieving multifunctionality and broadband microwave absorption, Chem. Eng. J. (2026). https://doi.org/10.1016/j.cej.2026.172882.

[4] J. Jiang, D. Lan, Y. Li, J. Yang, S. Deng, Q. He, Y. Wang, Construction of spherical heterogeneous interface on ZnFe2O4@C composite nanofibers for highly efficient microwave absorption, Ceram. Int. (2024). https://doi.org/10.1016/j.ceramint.2024.07.197.

[5] K. Wang, D. Deng, Y. Nie, C. Liu, H. Yu, T. Cui, B. Yao, B. Xia, Structural and compositional synergy in (CCWs/rGOAs):PANI composites for high-efficiency microwave absorption, Mater. Today Commun. (2026). https://doi.org/10.1016/j.mtcomm.2026.114686.

[6] B. Zhu, B. Zhou, R. Lin, M. Lv, X. Zhang, Study on microwave absorbing properties of reduced graphene oxide@Co/Fe81.5Si3B9P3C1Cu1Ti1.5 amorphous nanocrystalline composite, J. Magn. Magn. Mater. (2024). https://doi.org/10.1016/j.jmmm.2024.172590.

[7] Z. Ma, Y. Wang, Y. Zhang, C. Chen, D. Wu, K. Jiang, X. Han, X. Zhang, Defect-customized ZIF-derived nanostructured load FeC: Dual-function study on efficient Electro-Fenton degradation and microwave absorption, J. Environ. Chem. Eng. (2026). https://doi.org/10.1016/j.jece.2026.121296.

[8] Y. Li, M. Yuan, H. Liu, G. Sun, Assembly of CoNi nanoparticles on Ketjenblack carbon with superior performance and optimized impedance matching for electromagnetic wave

absorption, Journal of Alloys and Compounds (2019). https://doi.org/10.1016/j.jallcom.2019.05.231.

[9] W. Liao, Q. Wang, S. Liu, M. Jin, P. Luo, S. Xiao, X. Zhao, H. Lu, T. Yan, Carbon black/epoxy resin composites with tunable electromagnetic and mechanical synergy for high-performance microwave absorption, Mater. Sci. Eng. B (2025). https://doi.org/10.1016/j.mseb.2025.119102.

[10] J. Yan, X. Zhao, W. Chen, P. Liu, Zn-MOF-derived hierarchical carbon nanorods superstructures with tunable microwave absorption properties, Materials Research Bulletin (2023). https://doi.org/10.1016/j.materresbull.2023.112622.

[11] X. Jiang, Y. Ma, X. Qin, Y. Zhou, C. Ni, C. Hou, X. Yang, Y. Zhang, W. Du, X. Xie, CoFe loaded sponge carbon composites with size changes for microwave absorption: Effects of hydrogen pressure, Colloids Surf. A Physicochem. Eng. Aspects (2025). https://doi.org/10.1016/j.colsurfa.2025.139404.

[12] Y. Danli, R. Cheng, Preparation and microwave absorption properties of Fe3O4/activated carbon composites for naval ship stealth, J. Mater. Sci. Mater. Electron. (2025). https://doi.org/10.1007/s10854-025-16391-6.

[13] M.F. Elmahaishi, R.S. Azis, I. Ismail, K.K. Katibi, K.A. Matori, F.D. Muhammad, N.K. Saat, M.M.A. Kechik, L.K. Pah, C.S. Kien, N. Ibrahim, Synergistic high-performance electromagnetic and microwave absorption of BaFe12O19/NiFe2O4/carbon nanotube/graphene oxide nanocomposites, J. Mater. Sci. Mater. Electron. (2025). https://doi.org/10.1007/s10854-025-16403-5.

[14] S. Deng, X. Xu, C. Fan, Q. He, Y. Wang, Constructing pod-like ZnFe2O4@SiO2@C composite fibers network structure to enhance impedance matching for efficient microwave absorption, Colloid Surf. A-Physicochem. Eng. Asp. 727 (2025) 138430. https://doi.org/10.1016/j.colsurfa.2025.138430.

[15] X. Xue, L. Liang, X. Du, K. Jia, J. Xu, K. Zhang, G. Li, In-situ formed SiC onto coal gasification residue (semi coke) to fabricate oxidation process-tolerable SiC/Ni2Si/SC composite for efficient microwave absorption in hot-air environment, Fuel (2025). https://doi.org/10.1016/j.fuel.2025.134508.

[16] J. Zang, H. Li, Q. Zhu, Z. Wang, H. Bazaerbieke, L. Sun, M. Zhang, High efficiency

microwave absorption properties of α−SiCp/α−SiCnw/SiO2/C composites with multi−interface hybrid SiC nanowires prepared by heterogeneous nucleation−growth mechanism, J. Alloys Compd. (2025). https://doi.org/10.1016/j.jallcom.2025.178759.

[17] Y. Shen, F. Zhang, Y. Zhang, M. Dang, B. Li, J. Ma, X. Du, Ni/NiO/SiO2/C nanofibers with strong wideband microwave absorption and robust hydrophobicity, Appl. Surf. Sci. (2022). https://doi.org/10.1016/j.apsusc.2022.152964.

[18] G. Li, J. Gao, X. Du, K. Jia, K. Zhang, L. Liang, Construction and microwave absorbing properties of Fex Oy /C composites based on corncobs, Journal of Fuel Chemistry and Technology 53 (2025) 771–783. https://doi.org/10.3724/2097-213X.2024.JFCT.0028.

[19] Z. Li, H. Li, T. Ying, X. Liu, H. Li, Y. Shi, W. Chen, X. Zhang, What is the important factor affecting microwave absorption performance in corncob-derived carbon/Ni composites?, J. Phys. D: Appl. Phys. (2021). https://doi.org/10.1088/1361-6463/ac0d26.

[20] Y. Guo, Y. Ma, Z. Lai, M. Liu, Seawater desalination using photothermal particles made of corncob modified with polypyrrole in reverse gas-liquid-solid fluidized bed solar evaporator, Chem. Eng. Res. Des. (2026). https://doi.org/10.1016/j.cherd.2026.01.023.

[21] L. Wang, H. Guan, J. Hu, Q. Huang, C. Dong, W. Qian, Y. Wang, Jute-based porous biomass carbon composited by Fe3O4 nanoparticles as an excellent microwave absorber, J. Alloys Compd. (2019). https://doi.org/10.1016/j.jallcom.2019.06.351.

[22] T. Ying, J. Zhang, X. Liu, J. Yu, J. Yu, X. Zhang, Corncob-derived hierarchical porous carbon/Ni composites for microwave absorbing application, J. Alloys Compd. (2020). https://doi.org/10.1016/j.jallcom.2020.156662.

[23] Y. Dong, C. Li, S. Gao, M. Yu, G. Sun, 3D porous Fe4N/C via nitridation engineering for high-performance microwave absorption, Journal of Alloys and Compounds (2026). https://doi.org/10.1016/j.jallcom.2026.188388.

[24] G. Li, X. Xue, K. Jia, H. Kang, K. Zhang, L. Liang, Construction of SiO 2-SiC/C composite absorber based on coal hydrogenation semi coke, Ceram. Int. 50 (2024) 24638–24647. https://doi.org/10.1016/j.ceramint.2024.04.198.

[25] Q. Yu, Z. Zhang, Y. Tang, D. Zheng, H. Dai, Z. Cao, Multilayered graphene foam composites with a gradient distribution of Fe3O4 hollow microspheres for broadband microwave absorption, Ceram. Int. (2025). https://doi.org/10.1016/j.ceramint.2025.11.121.

[26] R. Zhang, X. Ye, S. Tan, Y. Wang, R. Li, E. He, Y. Ye, H. Wu, (CoCrFeCuNi)3O4@C-graphene/PLA composite material exhibits thin , wide-bandwidth, and excellent microwave absorption properties, Ceram. Int. 51 (2025) 62958–62970. https://doi.org/10.1016/j.ceramint.2025.11.034.

[27] N. Meftah, A. Hani, A. Merdas, Extraction and Physicochemical Characterization of Highly-pure Amorphous Silica Nanoparticles from Locally Available Dunes Sand, Chemistry Africa 6 (2023) 3039–3048. https://doi.org/10.1007/s42250-023-00688-2.

[28] Y. Liu, L. Wu, A. Chen, C. Xu, X. Yang, Y. Zhou, Z. Liao, B. Zhang, Y. Hu, H. Fang, Component Design of Environmentally Friendly High-Temperature Resistance Coating for Oriented Silicon Steel and Effects on Anti-Corrosion Property, Coatings 12 (2022) 959. https://doi.org/10.3390/coatings12070959.

[29] J. Chen, N. Xia, T. Zhou, S. Tan, F. Jiang, D. Yuan, Mesoporous Carbon Spheres: Synthesis, Characterization and Supercapacitance, Int. J. Electrochem. Sci. 4 (2009) 1063–1073.

[30] M.K. Mondal, N. Bhakta, M. Dalal, S. Sadhukhan, A. Banerjee, C.C. Dey, S. Das, P.K. Chakrabarti, Microwave absorption and magnetic properties of Ni-NiO-GO nanocomposites, J. Magn. Magn. Mater. (2025). https://doi.org/10.1016/j.jmmm.2025.172819.

[31] H. Zhao, Z. Liu, J. Hao, S. Zheng, Y. Cao, T. Liu, Y. Sun, Y. Du, 1D superstructure assembled from 2D carbon nanosheets for microwave absorption, J. Mater. Sci. Technol. (2025). https://doi.org/10.1016/j.jmst.2025.10.057.

[32] B. Lei, G. Wang, C. Li, Q. Fan, Z. Yang, Y. Li, C. Zhou, C. Kong, Rapid synthesis and enhanced microwave absorption of carbon-supported high-entropy metal oxide, J. Alloys Compd. (2024). https://doi.org/10.1016/j.jallcom.2024.176964.

[33] Y. Chen, Y. Jiang, F. Gan, Y. Zhong, Q. Yao, L. Cheng, Z. Lu, H. Qin, J. Wang, Y. Huang, Construction of dandelion-like FeCo/Co@C composites with improved microwave absorption performance, J. Mater. Sci.-Mater. Electron. 36 (2025) 1959. https://doi.org/10.1007/s10854-025-16001-5.

[34] Y. Wang, L. Liang, B. Zhu, Y. Tian, G. Li, Economical preparation of Fe3O4/C/CG and Fe/C/CG composites as microwave absorbents by recycling of coal gangue, Mater. Res. Bull. (2021). https://doi.org/10.1016/j.materresbull.2021.111573.

[35] F. Al Ma'Mari, M. Rogers, S. Alghamdi, T. Moorsom, S. Lee, T. Prokscha, H. Luetkens, M.

Valvidares, G. Teobaldi, M. Flokstra, R. Stewart, P. Gargiani, M. Ali, G. Burnell, B.J. Hickey, O. Cespedes, Emergent magnetism at transition-metal-nanocarbon interfaces [Applied Physical Sciences], Proc. Natl. Acad. Sci. U.S.A. (2017). https://doi.org/10.1073/pnas.1620216114.

[36] B. Rosales-Reina, G. Cruz-Quesada, N. Padilla-Postigo, M. Irigoyen-Razquin, E. Alonso-Martínez, M.V. López-Ramón, M. Espinal-Viguri, J.J. Garrido, Tunability of Hybrid Silica Xerogels: Surface Chemistry and Porous Texture Based on the Aromatic Precursor, Gels (2023). https://doi.org/10.3390/gels9050382.

[37] D. Chen, K. Cen, X. Zhuang, Z. Gan, J. Zhou, Y. Zhang, H. Zhang, Insight into biomass pyrolysis mechanism based on cellulose, hemicellulose, and lignin: Evolution of volatiles and kinetics, elucidation of reaction pathways, and characterization of gas, biochar and bio-oil, Combust. Flame 242 (2022) 112142. https://doi.org/10.1016/j.combustflame.2022.112142.

[38] M. Elma, A. Sumardi, A. Paramita, A. Rahma, A.E. Lestari, D.H.Y. Yanto, S. Hadi, Z.L. Assyaifi, Sunardi, Y. Raharjo, Physicochemical Properties of Mesoporous Organo-Silica Xerogels Fabricated through Organo Catalyst, Membranes 11 (2021) 607. https://doi.org/10.3390/membranes11080607.

[39] K. Papachristopoulou, N.A. Vainos, Systolic Nanofabrication of Super-Resolved Photonics and Biomimetics, Nanomaterials (2020). https://doi.org/10.3390/nano10122418.

[40] G. Ji, C. Ma, S. Jin, N. Song, W. Li, Facile synthesis of $MnFe_2O_4$ nanoparticles/biomass-derived porous carbon composites with superior microwave absorption performance, Mater. Today Commun. (2025). https://doi.org/10.1016/j.mtcomm.2025.114165.

[41] Y. Cai, H. Yu, L. Cheng, Y. Yuan, S. Guo, Z. Hu, Y. Wang, D. Chen, J. Liu, H. Yuan, Microwave absorption properties of one-step formed CNTs/Fe3O4-carbonyl iron superflexible buckypaper by directional pressure filtration, Ceram. Int. 50 (2024) 51128–51138. https://doi.org/10.1016/j.ceramint.2024.10.025.

[42] M. Wang, D. Li, Z. Yang, D. Guo, B. Wang, J. Xiang, K. Zhai, Y. Cheng, F. Wen, A. Nie, Z. Liu, C. Mu, Architectures engineering a porous carbon core with a metal alloys nanoparticles decorated porous carbon shell for ultra-wideband microwave absorption and strong reflection loss, J. Alloy. Compd. 1055 (2026) 186523. https://doi.org/10.1016/j.jallcom.2026.186523.

[43] H. Yang, S. Qiu, L. Wang, Q. Li, R. Che, Heterogeneous interface engineering in

FexOy@C@Expanded graphite array structure with confined magnetic coupling to boost microwave absorption, Carbon 242 (2025) 120434. https://doi.org/10.1016/j.carbon.2025.120434.

[44] M. Zhang, X. Qian, Q. Zeng, Y. Zhang, H. Cao, R. Che, Hollow microspheres of polypyrrole/magnetite/carbon nanotubes by spray-dry as an electromagnetic synergistic microwave absorber, Carbon (2021). https://doi.org/10.1016/j.carbon.2021.01.013.

[45] B. Ma, Y. Huang, Z. Nie, X. Qiu, D. Su, G. Wang, J. Yuan, X. Xie, Z. Wu, Facile synthesis of Camellia oleifera shell-derived hard carbon as an anode material for lithium-ion batteries†, RSC Adv. (2019). https://doi.org/10.1039/c9ra03345a.

[46] M.S. Choi, H.G. Na, J.H. Bang, S.-W. Choi, S.S. Kim, K.H. Lee, H.W. Kim, C. Jin, Interface treatment using amorphous-carbon and its applications, Sci. Rep. (2020). https://doi.org/10.1038/s41598-020-61141-9.

[47] Z. Huang, Y. Yao, Z. Pang, Y. Yuan, T. Li, K. He, X. Hu, J. Cheng, W. Yao, Y. Liu, A. Nie, S. Sharifi-Asl, M. Cheng, B. Song, K. Amine, J. Lu, T. Li, L. Hu, R. Shahbazian-Yassar, Direct observation of the formation and stabilization of metallic nanoparticles on carbon supports, Nat Commun 11 (2020) 6373. https://doi.org/10.1038/s41467-020-20084-5.

[48] F.H. Shareef Radha, M.T. Kareem, O.Gh. Abdullah, Atmosphere-dependent synthesis and crystallization behavior of silica nanoparticles derived from rice husk biomass, RSC Adv. 16 (2026) 16874–16886. https://doi.org/10.1039/D6RA00367B.

[49] T. Manimekala, R. Sivasubramanian, M.A. Dar, G. Dharmalingam, Crafting the architecture of biomass-derived activated carbon *via* electrochemical insights for supercapacitors: a review, RSC Adv. 15 (2025) 2490–2522. https://doi.org/10.1039/D4RA07682F.

[50] C. Ania, T.J. Bandosz, D. Cazorla-Amorós, M.F.R. Pereira, Advancing Porous Carbons: Understanding the Importance of Surface Chemistry for the Energy–Environment Nexus, Chem. Rev. 126 (2026) 2678–2800. https://doi.org/10.1021/acs.chemrev.5c00719.

[51] Z. Lou, H. Han, Y. Shi, Z. Wang, M. Zhang, L. Li, H. Yan, L. Xu, Q. Zhang, Y. Li, X. Mo, W. Lu, H. Lv, Atomic-Scale Customization of Oriented Dipolar Defects in Amorphous Carbon via Nanoparticle-Templated Phase Engineering, Adv Funct Materials 36 (2026) e20584. https://doi.org/10.1002/adfm.202520584.

[52] K. Jin, X. Li, Y. Shi, C. Wang, W. Guo, K. Tian, H. Wang, Defects in Discrete Nanocrystals

of Thin-Shelled Amorphous Carbon Induced Dipole Polarization for Boosting Broadband Response, Adv Funct Materials 36 (2026) e14258. https://doi.org/10.1002/adfm.202514258.

[53] E.F. Sheka, A Neoteric View of sp2 Amorphous Carbon, Nanomaterials 13 (2023) 1648. https://doi.org/10.3390/nano13101648.

[54] A.C. Ferrari, J. Robertson, Raman spectroscopy of amorphous, nanostructured, diamond–like carbon, and nanodiamond, Philosophical Transactions of the Royal Society of London. Series A: Mathematical, Physical and Engineering Sciences 362 (2004) 2477–2512. https://doi.org/10.1098/rsta.2004.1452.

[55] M. Wei, L. Zhang, Y. Xiong, J. Li, P. Peng, Nanopore structure characterization for organic-rich shale using the non-local-density functional theory by a combination of N2 and CO2 adsorption, Microporous Mesoporous Mat. 227 (2016) 88–94. https://doi.org/10.1016/j.micromeso.2016.02.050.

[56] J. Yan, Y. Wang, W. Liu, P. Liu, W. Chen, Two-Dimensional Metal Organic Framework derived Nitrogen-doped Graphene-like Carbon Nanomesh toward Efficient Electromagnetic Wave Absorption, Journal of Colloid and Interface Science (2023). https://doi.org/10.1016/j.jcis.2023.04.040.

[57] Y. Shen, C. Zhao, X. Wang, Q. Yu, F. Zhou, Microwave absorption and fast-response self-lubricating coating based on the PAO6@SiO2@Ppy microcapsules, Tribol. Int. 214 (2026) 111229. https://doi.org/10.1016/j.triboint.2025.111229.

[58] Y. Lu, B. Hong, J.C. Xu, J. Li, Y.X. Zeng, X.L. Peng, S. Qiu, X.Q. Wang, Improved microwave absorption properties of CoFe2O4/AC nanocomposites from matching electromagnetic characteristics, J. Magn. Magn. Mater. 614 (2025) 172688. https://doi.org/10.1016/j.jmmm.2024.172688.

[59] B. Ye, H. Zhang, X. Hong, K.S. Hui, B. Mu, J. Yang, Direct synthesis of bimetallic Co/Zn-MOF-derivative@mica composite with high microwave absorption performance and pearlescent properties, Surf. Interfaces 58 (2025) 105744. https://doi.org/10.1016/j.surfin.2025.105744.

[60] Y. Liu, J. Zhang, Q. Gao, R. Hu, Fabrication of hollow Fe3O4 microspheres encapsulated by single-walled carbon nanohorns for high-performance microwave absorption, Ceram. Int. 50 (2024) 55879–55891. https://doi.org/10.1016/j.ceramint.2024.10.470.

[61] H. Zhao, Y. Cheng, W. Liu, L. Yang, B. Zhang, L.P. Wang, G. Ji, Z.J. Xu, Biomass-Derived Porous Carbon-Based Nanostructures for Microwave Absorption, Nano-Micro Lett. 11 (2019) 24. https://doi.org/10.1007/s40820-019-0255-3.

[62] J. Yan, H. Jia, L. Zhou, Z. Wang, H. Wang, Tunable Complex Permittivity and Strong Microwave Absorption Properties of Novel Dielectric-Conductive ZnO/C Hybrid Composite Absorbents, Metals 13 (2023) 1220. https://doi.org/10.3390/met13071220.

[63] X. Mu, D. Lingli, Y. Guo, R. Zhou, X. Guo, X. Jian, X. Zhao, Covalent bonding-designed Ti3C2Tx@Fe3O4@SiO2</sub > nanocomposites for high-efficiency microwave absorption, Ceram. Int. 51 (2025) 41145–41156. https://doi.org/10.1016/j.ceramint.2025.06.338.

[64] J. Li, Z. Wu, Y. Xu, W. Wang, D. Niu, J. Guan, J. Qi, Z. Huang, N-self-doped coffee grounds-derived porous carbon for lightweight and high-performance microwave absorption, Diam. Relat. Mat. 159 (2025) 112820. https://doi.org/10.1016/j.diamond.2025.112820.

[65] R. Feng, D. Lan, Y. Li, Y. He, Q. He, Y. Wang, Multiphase magnetic array-anchored layered Fe3O4/FeO/C composites with magnetic coupling effect for highly efficient microwave absorption, Ceram. Int. 50 (2024) 55461–55469. https://doi.org/10.1016/j.ceramint.2024.10.405.

[66] M. Liu, B. Wang, Y. Hou, Y. Wang, B. Li, D. Fu, J. Chen, K. Liu, T. Wan, Q. Han, X. Lu, C. Guo, S. Wei, A facile high-temperature mechanochemical preparation of zinc ferrite powder for microwave absorption, Mater. Sci. Eng. B-Adv. Funct. Solid-State Mater. 323 (2026) 118812. https://doi.org/10.1016/j.mseb.2025.118812.

[67] R. Zhang, P. Zu, Y. Yan, G. Zhang, Heterojunction engineering of large-sized Ti3C2Tx MXene with ZnO for enhanced high-frequency microwave absorption and thermal conductivity, Compos. Sci. Technol. 271 (2025) 111321. https://doi.org/10.1016/j.compscitech.2025.111321.

[68] T. Zhang, W. He, Y. Ma, H. Guo, High-temperature microwave absorption of SrZrO3-based coatings: Mechanisms and enhanced absorption by high-impedance surface, Surf. Coat. Technol. 498 (2025) 131793. https://doi.org/10.1016/j.surfcoat.2025.131793.

[69] M. Liu, B. Wang, Y. Wang, D. Fu, Y. Chang, B. Li, K. Liu, X. He, J. Chen, S. Wei, Q. Han, Structural, magnetic and microwave absorption performances of MnxZn(1-x)Fe2O4 nanopowders via high-temperature mechanochemical method, Ceram. Int. 51 (2025) 2898–

2913. https://doi.org/10.1016/j.ceramint.2024.11.267.

[70] Q. Ji, L. Yang, H.-Y. Wang, N. Jamaluddin, J. Matmin, Y. Zhu, Multifunctional polyimide/rGO aerogels with stain-responsive ultrabroadband microwave absorption properties and thermal insulation, Compos. Commun. 58 (2025) 102550. https://doi.org/10.1016/j.coco.2025.102550.

[71] Y. Liu, J. Zhang, S. Yuan, W. Cao, X. Lu, Y. Sheng, W. Gu, Y. Kuang, P. Zhou, Hierarchical C-CoS2@MoS2 with core-shell structure boosting interfacial polarization for optimizing microwave absorption, J. Alloy. Compd. 1039 (2025) 183144. https://doi.org/10.1016/j.jallcom.2025.183144.

[72] X. Fang, Q. Wu, Z. Gu, S. Yin, H. Ma, C. Zhou, T. Li, L. Liu, R. Zuo, Fabrication of Al2O3-based composite ceramics with mesocarbon microbeads as absorbent for enhanced microwave absorption, Ceram. Int. 51 (2025) 39886–39898. https://doi.org/10.1016/j.ceramint.2025.06.222.

[73] A. Zhang, W. Wang, R. Cui, A. Du, J. Jia, Y. Huang, C. Wan, R. Ma, Multifunctional Ti3C2Tx/Fe3O4/glass fiber paper composites for flexible microwave absorption materials with ultralow filling ratio, Ceram. Int. 51 (2025) 824–835. https://doi.org/10.1016/j.ceramint.2024.11.067.

[74] D. Ma, Y. Zhang, S. Gao, Ultrathin MgFe2O4/coal gasification fine slag composites for efficient electromagnetic wave absorption and performance optimization, Ceramics International (2025). https://doi.org/10.1016/j.ceramint.2025.05.078.

[75] J. Shu, J. Zhou, B. Cao, S. Lu, D. Ding, Z. Zi, Magneto-dielectric synergy design CoFe2O4 decorated MXene composites for broadband electromagnetic wave absorption, Diam. Relat. Mat. 161 (2026) 113041. https://doi.org/10.1016/j.diamond.2025.113041.

[76] S. Huang, X. Dong, L. Pei, X. Zhang, Enhancing interface polarization by interface engineering of MoSe2/FeSe to achieve efficient microwave absorption, Mater. Today Phys. 57 (2025) 101819. https://doi.org/10.1016/j.mtphys.2025.101819.

[77] R. Phani, S. Sahu, R.C. Gurrala, P. Dobbidi, K. Raidongia, B.S. Latha, B.K. Babu, N. Annapurna, Leveraging synergistic interfaces in NiO and NiO/rGO heterostructures for enhanced microwave absorption, Surf. Interfaces 56 (2025) 105617. https://doi.org/10.1016/j.surfin.2024.105617.

[78] W. Deng, T. Li, H. Li, X. Liu, A. Dang, Y. Liu, H. Wu, Controllable graphitization degree of

carbon foam bulk toward electromagnetic wave attenuation loss behavior, J. Colloid Interface Sci. (2022). https://doi.org/10.1016/j.jcis.2022.03.071.

[79] J. Wang, Y. Chen, H. Rao, X. An, K. Nan, Y. Wang, Constructing Schottky contacts via vertical growth of SnS2 nanosheets on hollow microspheres for efficient microwave absorption, J. Mater. Sci. Technol. 232 (2025) 147–155. https://doi.org/10.1016/j.jmst.2025.01.037.

[80] G. Li, Y. Huang, J. Zhang, K. Li, K. Zhang, L. Liang, Preparation of FexSiy/SiC/C composite microwave absorbents by fly ash and coal gasification residue, Ceram. Int. 51 (2025) 35734–35743. https://doi.org/10.1016/j.ceramint.2025.05.297.

[81] X. Xu, L. Miao, K. Sun, Preparation and microwave absorption performance of silicon carbide/ platanus catkin-derived carbon composites, Ceram. Int. 52 (2026) 26058–26067. https://doi.org/10.1016/j.ceramint.2026.04.065.

[82] Y. Li, L. Wang, T. Yu, G. Wen, X. Tang, W. Chang, Q. Li, J. Wang, Facile Fabrication of Co-Doped Porous Carbon Derived from Coal Hydrogasification Semicoke/ZIF-67 for High-Performance Microwave Absorption, ACS Appl. Mater. Interfaces 17 (2025) 61038–61049. https://doi.org/10.1021/acsami.5c15462.

[83] X. Zheng, X. Li, F. Lv, Core-shell heterostructured nanofibers consisting of graphite-coated FeNi nanoparticles embedded into N-doped carbon nanofibers as an efficient microwave absorber, Mater. Today Commun. 48 (2025) 113662. https://doi.org/10.1016/j.mtcomm.2025.113662.

[84] Y. Zhang, S. Gao, X. Zhang, D. Ma, C. Zhu, J. He, Structural and microwave absorption properties of CoFe2O4/residual carbon composites, Int J Miner Metall Mater 32 (2025) 221–232. https://doi.org/10.1007/s12613-024-2849-0.

[85] D. Wu, S. Deng, Y. Wang, J. Wen, L. Ren, Q. He, Hierarchical porous carbon fibers for broadband and tunable high-performance microwave absorption, Mater. Res. Bull. 172 (2024) 112653. https://doi.org/10.1016/j.materresbull.2023.112653.

[86] Z. Lou, Q. Wang, U. Kara, R.S. Mamtani, X. Zhou, H. Bian, Z. Yang, Y. Li, H. Lv, S. Adera, X. Wang, Biomass-Derived Carbon Heterostructures Enable Environmentally Adaptive Wideband Electromagnetic Wave Absorbers, Nano-Micro Lett. 14 (2022) 11. https://doi.org/10.1007/s40820-021-00750-z.

[87] R. Zhang, J. Qiao, X. Zhang, Y. Yang, S. Zheng, B. Li, W. Liu, J. Liu, Z. Zeng, Biomass-

derived porous carbon for microwave absorption, Mater. Chem. Phys. 289 (2022) 126437. https://doi.org/10.1016/j.matchemphys.2022.126437.

[88] Z. Li, K. Peng, N. Ji, W. Zhang, W. Tian, Z. Gao, Advanced mechanisms and applications of microwave-assisted synthesis of carbon-based materials: a brief review, Nanoscale Adv. 7 (2025) 419–432. https://doi.org/10.1039/D4NA00701H.

[89] Y. Ai, R. Xing, R. Huang, J. Kong, R. Su, Biomass-derived fire-retardant porous carbon towards efficient electromagnetic wave absorption and shielding, Carbon 227 (2024) 119268. https://doi.org/10.1016/j.carbon.2024.119268.

[90] B. Zhu, X. Wang, W. Mu, X. Sun, Y. Wang, H. Wei, P. Shi, H. Hao, D. Wang, G. Li, G. Wang, Recycling paper mill sludge to prepare low-cost Ni-modified carbon/silica composite for efficient microwave absorption, Acta Physico-Chimica Sinica (2026). https://doi.org/10.1016/j.actphy.2026.100417.

Acknowledgements

This work was supported by the National Nature Science Foundation of China (52572138, 52378360, 51802212), the Central Guidance on Local Science and Technology Development Fund of Shanxi Province (YDZJSX2024D057), the patent conversion project (C2025041).

Funding

The National Nature Science Foundation of China,52572138, 52378360, 51802212, The Central Guidance on Local Science and Technology Development Fund of Shanxi Province, YDZJSX2024D057, The patent conversion project, C2025041.

Competing Interests

The authors declare no competing interests.

Author Contributions

Yufei Wu: Writing - original draft, Data curation, Formal analysis, Conceptualization, Methodology. Jinhao Hu: Methodology, Investigation, Formal analysis. Jinyan Li: Validation, Investigation, Data curation. Liping Liang: Writing - review & editing, Visualization, Supervision, Project administration, Conceptualization.

Yirong Huang: Methodology, Investigation, Kun Jia: Supervision, Project administration. Xiaoqiang Dong: Data curation, Investigation. Kewei Zhang: Methodology, Formal analysis. Guomin Li: Writing - review & editing, Visualization, Supervision, Project administration, Investigation, Formal analysis.

Supplementary information

Supplementary data associated with this article can be found in the online version. The SEM images of the bare corn cob sample (a) and SiO_2/C-900-40 (b) are shown in Fig. S1, the EDS spectra of SiO_2/C-700-40 and SiO_2/C-800-40 are shown in Fig. S2, the reflection loss and effective absorption bandwidth curves of SiO_2/C-600-40 are presented in Fig. S3, the EDS spectra of SiO_2/C-900-20 and SiO_2/C-900-60 are shown in Fig. S4, the frequency-dependent curves of the real part of the dielectric constant, imaginary part of the dielectric constant, and Cole–Cole plots for SiO_2/C-900-*Y* (*Y* = 20, 40, 60) are shown in Fig. S5.

Supplementary Files

This is a list of supplementary files associated with this preprint. Click to download.

- SupplementaryMaterial.docx